Journal of Manufacturing Processes 154 (2025) 236–248

Contents lists available at ScienceDirect

Journal of Manufacturing Processes

journal homepage: www.elsevier.com/locate/manpro

Optimal-transport-based geometry modeling for material extrusion additive manufacturing

Siqi Chen [a], Shuai Liu [a], Shuaiyin He [a], Molong Duan [a,b,*]

[a] Department of Mechanical and Aerospace Engineering, The Hong Kong University of Science and Technology, Hong Kong

[b] HKUST Shenzhen-Hong Kong Collaborative Innovation Research Institute, Futian, Shenzhen, China

GRAPHICAL ABSTRACT

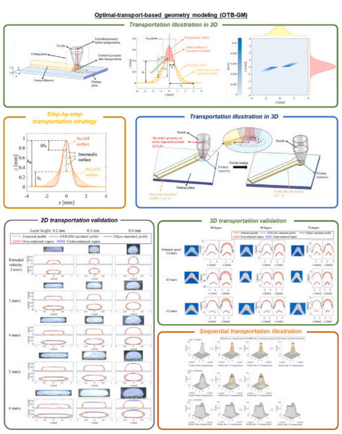

ARTICLE INFO

Keywords:
Additive manufacturing
Profile modeling
Optimal transport

ABSTRACT

Material extrusion additive manufacturing is increasingly adopted in the automotive, aerospace, and medical industries for its capability to create complex features at low cost. Despite high flexibility, parts fabricated with the material extrusion method continue to suffer from geometric inaccuracies and dimensional instability, particularly when manufacturing structures that require high geometric fidelity, such as those with intricate internal channels. To enhance the precision and stability of the material extrusion process, geometry modeling methods based on manufacturing parameters have been introduced. Researchers have employed physical models and neural networks to predict the geometry of printed parts. However, physical modeling is often characterized by high complexity and significant computational demands, while neural networks require a substantial amount of measurement data, resulting in a high cost in experiments. The high computation load and measurement data demand of existing geometry prediction methods prevent their widespread adoption in industrial settings, as they lead to prohibitively long simulation times and the inability to support real-time process optimization. To close the research gap, we propose an optimal-transport-based geometry modeling (OTB-GM) method for the material extrusion system. The proposed OTB-GM models the ironing effects of the moving nozzle for generating the final extruded profile, by minimizing the energy consumption of the transportation process. The OTB-GM

* Corresponding author at: Department of Mechanical and Aerospace Engineering, The Hong Kong University of Science and Technology, Hong Kong.
E-mail address: duan@ust.hk (M. Duan).

https://doi.org/10.1016/j.jmapro.2025.09.042
Received 9 June 2025; Received in revised form 2 September 2025; Accepted 16 September 2025
Available online 3 October 2025

begins by initializing the profile prior to ironing, resembling the shape of a Gaussian distribution. In constructing the model, we take into account the material's viscous resistance, changes in gravitational potential energy, and modifications to the surface geometry during ironing. We derive the formula of OTB-GM in two dimensions (2D) and three dimensions (3D) for modeling steady (like line) and dynamic (like corner) extrusion conditions, respectively. To validate the modeling accuracy of the proposed OTB-GM method, the straight line and corner parts are printed for 2D and 3D verification, respectively. Compared with the conventional ellipse geometry modeling method, the proposed OTB-GM reaches higher accuracy in both 2D and 3D validation cases.

1. Introduction

Additive manufacturing holds an essential position in modern industry, with the capability of rapid prototyping and producing complex internal structures [1,2]. With the distinct advantage of additive manufacturing, industries increasingly adopt it for fabricating functional parts, while the need for reliability and repeatability during the manufacturing process becomes crucial. However, the current additive manufacturing system still suffers from low product stability and consistency [3,4], impacting both its mechanical properties and dimensional precision in the final product. Thus, the bead geometry modeling and prediction method with given fabrication parameters (like nozzle moving speed and extrusion speed) is introduced for enhancement. Kechagias et al. [5,6] investigated the impact of process parameters (like layer thickness, infill rate, material flow rate, printing temperature, and extrusion velocity) on the surface roughness and the bonding quality of printed parts. Kumar et al. [7] reported the surface roughness and tensile strength for acrylonitrile butadiene styrene (ABS) under cold weather conditions, with respect to layer thickness, extrusion temperature, and raster angle. By modeling the geometry generation process of the printing material, the manufacturers can predict and mitigate potential issues such as extrusion inaccuracy, warping, and layer adhesion failures, thereby reducing material waste caused by printing failure and enhancing the sustainability of the manufacturing process [7]. Furthermore, effective geometry modeling brings the potential for the real-time optimization of printing parameters, which can significantly reduce material waste and production time.

For the convenience of expressing bead geometry during modeling, various methods for parameterizing bead geometry have been introduced. Comminal et al. [8] adopted oblong and cuboid shapes for fitting the cross-section of the extruded filament. Wang et al. [9] applied the ellipsoid shape assumption to the extrusion material for surface roughness investigation of the printed part. As the parameterization methods were introduced, researchers were able to propose various kinds of bead geometry modeling methods. Serdeczny et al. [10] introduced the relationship between extrusion geometry and nozzle diameter, layer height, and printing speed by Computational fluid dynamics (CFD) simulation. Huang et al. [11] used convolution formulation to facilitate the prediction of three-dimensional (3D) printing accuracy. Haghbin et al. [12] investigated the effect of geometric models on the width and height of the extruded roads. Tashi et al. [13] elucidated the characteristics of the parameters used in the recursive process as well as its ability in geometric modeling and 3D printing of 3D shapes. Sutjipto et al. [14] used online image analysis techniques to generate the thickness and intersection deviation data. Nuchitprasitchai et al. [15] provided a bead geometry reconstruction and deviation modeling method by overlapping two-dimensional (2D) intensity measurements with relaxed camera positioning requirements. Friedrich and Begley [16] investigated how the extrusion pressure and the stand-off distance influence the filament shape and its stability. Ferraris et al. [17] captured the temperature profiles of printed material to predict the bead geometry after bonding. Borish et al. [18,19] built a bead-filling inaccuracy estimation method by processing the data from the thermal camera and profilometer. By applying the Kalman filter and Canny filter to the inertial measurement unit (IMU) and accelerometer, Gao et al. [20] estimated the height of the bead geometry by the printer motion data. However, most of the existing modeling methods are with high complexity and have large computational consumption.

Neural network (NN) method has also been widely used in geometry modeling methods. Li et al. [21] predicted the intrinsic geometry of 3-dimensional printed parts by sending in situ metrology data to the conditional adversarial network (CAN). Sharma et al. [22] presented the dimensional deviations in parts produced by the MEX technique and demonstrated the effectiveness of a supervised learning model in predicting deviations based on processing parameters. Charalampous et al. [23] provided a machine learning-based regression model that correlates layer height, printing speed, and printing temperature with the dimensional deviations of specimens produced via MEX technology. Ntousia et al. [24] presented a framework for predicting errors and failures in additive manufacturing by introducing a three-hidden-layer neural network for estimating dimensional deviation and the probability of successful fabrication. Wang et al. [25,26] designed an inspection system with a rotating camera for surface image capturing, and built a corresponding convolutional neural network (CNN)-based image processing model for surface defects classification. Becker et al. [27] employed long short-term memory neural networks (LSTM) to generate printed bead height from collected acoustic signals recorded near the extruder. Li et al. [28] gave a surface roughness prediction model based on the ensemble learning algorithm (including random forest, adaptive boosting, classification and regression trees, support vector regression, ridge regression, and random vector functional link network), by using the data from thermocouples, infrared temperature sensors, and accelerometers as the input. Schlegel et al. [29] trained a predictive model by self-learning algorithm for the product geometry deviation forecast. Zhu et al. [30] trained a CNN-based learning method for geometry deviation prediction, taking the computed tomography (CT) data as the input. However, training NN models necessitates a substantial amount of data obtained from advanced measurement techniques, such as CT, which incurs significant expenses and time commitments for experiments.

To close the research gap, we build an optimal-transport-based geometry modeling (OTB-GM) method for material extrusion (MEX) 3D printing in this paper. The proposed OTB-GM method generates the geometry profile of extruded materials based on analyzing the ironing effect of the nozzle during fabrication. As the ironing effect is involved with the change of material position, optimal transport is introduced for problem-solving by minimizing the energy consumption of the transportation process. The proposed OTB-GM considers the viscous drag, the gravitational potential energy change, and the surface shape modification during the material transportation process. In particular, the proposed methodology provides the following main contributions:

- The OTB-GM method is derived in 2D and 3D fields. The derivation of OTB-GM starts from assuming the profile before transportation resembles a Gaussian distribution, and following the minimal energy-consuming assumption, the final profile after transportation is calculated.
- The performance of the proposed OTB-GM method is estimated in 2D and 3D by printing the straight line part and the corner part, respectively. The geometry prediction result of OTB-GM is compared with that of the standard ellipse method.

The remainder of the paper is structured as follows: Section 2

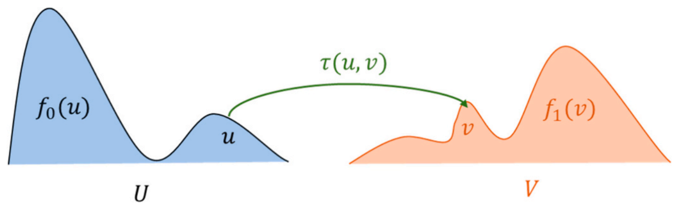

Fig. 1. Illustration of the profile before and after the transport.

introduces the background of the optimal transport. The formulation method of the optimal transport is described in this section. Section 3 derives the OTB-GM method in 2D and 3D, for processing the steady and dynamic printing processes, respectively. This section starts by discussing the Gaussian distribution-based geometry parameterization method for the printed material before being ironed by the nozzle. With the profile before ironing established, the methodology for modeling the nozzle ironing effect is proposed, resulting in the generation of the profile after ironing. As the modeling method is fully built, the OTB-GM method is constructed. Section 4 validates the capability of the proposed method in both 2D and 3D fields, by printing line parts and corner parts, respectively. The geometry estimation accuracy of the proposed OTB-GM method is evaluated and compared with that of the conventional ellipse modeling method. Section 5 is the conclusion.

2. The background of optimal transport

Optimal transport (OT) is a mathematical theory that focuses on the most efficient way to transport mass from one distribution to another [31]. This concept was first formulated by Gaspard Monge in the 18th century, aiming to minimize the cost of transporting soil from one location to another. The fundamental problem of OT is framed as finding a transport map to transform the mass from one place to another in the most cost-effective way. Define the profile before and after the transport as $f_0(u)$ and $f_1(v)$, respectively, as Fig. 1 shows. During the transportation process, the mass transported from position u to position v is defined as

$$\Delta m_{u,v} = \tau(u,v). \tag{1}$$

Thus, the final mass $f_1(v)$ satisfies the following distribution

$$f_1(v) = f_0(v) + \int_U \tau(u,v)du. \tag{2}$$

Following the mass conservation, the transport map satisfies

$$\int_V \tau(u,v)dv = f_0(u). \tag{3}$$

To enable efficient transportation, the total transportation energy E_t is incrementally calculated by integrating the distance-related energy, multiplied by the mass being transported, i.e.,

$$E_t = \iint_{U,V} e(u,v)\tau(u,v)dudv. \tag{4}$$

where $e(u,v)$ is the distance-related energy for transporting unit weight from u to v. In classical OT formulations, the positive definite distance from u to v is typically exploited in practical formulations. Assuming in the transport map, the capacity of the position v is limited. Define the maximum allowance weight in the v of the final profile as $M_w(v)$. Thus, the OT problem is finalized to the following minimization equation,

$$\begin{aligned} &\tau(u,v) = \operatorname{argmin}\{E_t\}, \\ &\text{s.t.} \int_V \tau\left(u,v\right)dv = f_0(u), \\ &f_1(v) \leqslant M_w(v). \end{aligned} \tag{5}$$

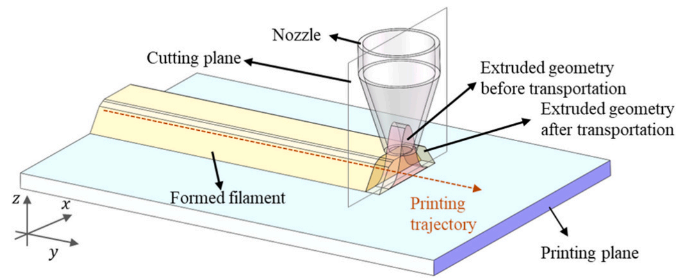

Fig. 2. Illustration of the extrusion and the transportation process in 2D modeling.

The illustration of the profile before and after the transportation is shown in Fig. 1. Linear or quadratic programming is typically used to solve the optimal transportation problem, depending on the specific form of the cost function.

3. Optimal-transport-based geometry modeling for the MEX process

In the MEX process, the deposited material is first deposited on the base layer and then ironed by the moving nozzle. This deposition and ironing process shapes the final bead geometry, creates a relatively flat surface for the deposited top layer, and is critical for the deposited geometry. This deposition and ironing process resembles the classical transport problem as the initial deposition is typically assumed to follow a Gaussian distribution [32–34], while the profile is ironed by the moving nozzle while the extruded material is transported. This transport process could be formulated and described under the optimal transport framework. The proposed OTB-GM method takes into account the changes in gravitational potential energy, the viscous resistance of the flowing material, and variations in surface energy during transportation. This method models both the cross-section profile and the three-dimensional profile of the extruded material using 2D and 3D optimal transport, respectively. The cross-section profile modeling method is applied to straight-line printing parts with a constant extrusion rate, while the three-dimensional modeling method is utilized for fabrication processes involving dynamic nozzle movement and varying extrusion trajectories (like corners). Considering that for commonly used thermoplastic printing materials in the MEX method, their thermal expansion is typically lower than 100×10^{-6}/K, a temperature drop of 200 °C results in only a 0.02 % dimensional shrinkage. While in commercial MEX printers, the typical dimensional accuracy error can reach 0.5 %. Therefore, the thermal expansion in the proposed OTB-GM method is omitted.

3.1. *Material extrusion cross-section profile modeling with 2D optimal transport*

Considering the material extrusion situation in Fig. 2, the nozzle, with the radius r_n, is printing along a straight-line trajectory, which is parallel to the y axis. The printing trajectory is defined as $[x(t), y(t)]^\top$. The distance between the nozzle and the printing plane is defined as h_l. The printing processing is with constant nozzle speed v_n and extrusion speed v_e. Assuming that during a specific time interval $[t_0, t_1]$, the volume of extruded material is V_m. As the nozzle is moving at a constant speed along the y axis and the extrusion speed remains unchanged, the profile of extruded material in the xz plane should be equivalent to each other. For the simplification of derivation, the extrusion profile is sliced along the cutting plane, which is parallel to the xz plane and perpendicular to the y axis (as illustrated in Fig. 3(a)). Assume the geometry condition of the cutting plane is collected at the sample time t_c, and the t_c satisfies $t_0 \leqslant t_c \leqslant t_1$. At the time t_c, the volume of extruded material is $V_m/(t_1 - t_0)$, and the shape of the extruded material is assumed to resemble a

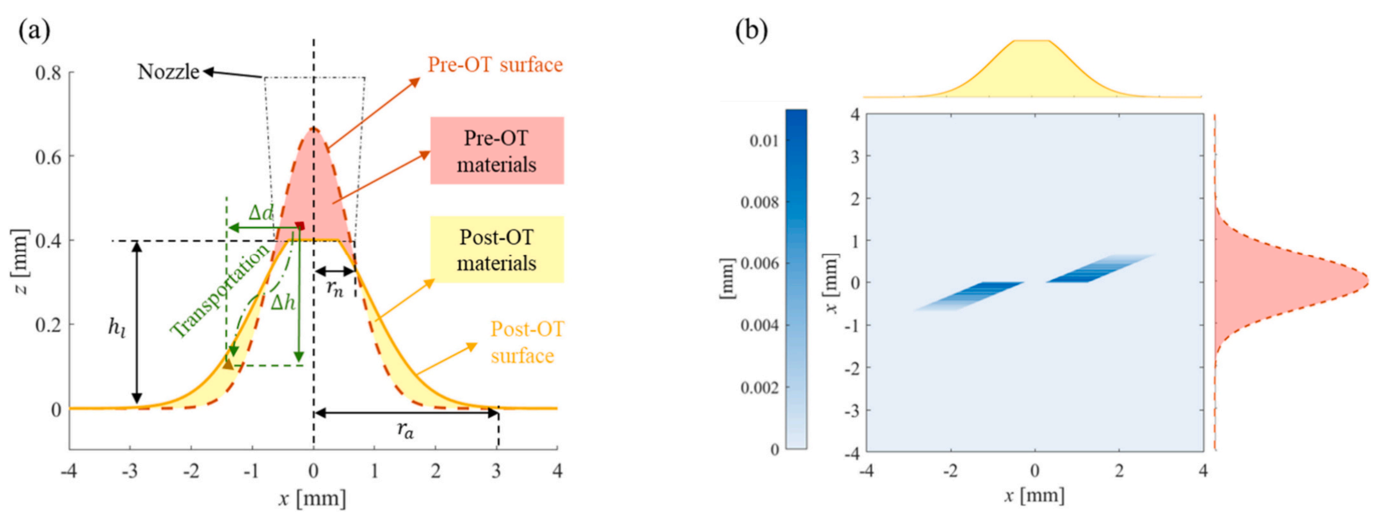

Fig. 3. (a) The transportation illustration in 2D modeling, and (b) the transport map illustration.

Gaussian distribution [32–34]. Define a and b as the coefficient in the Gaussian distribution. The height profile $f_0(x)$ of extruded material at t_c is expressed as

$$f_0(x) = \frac{b}{\sqrt{2\pi}} e^{-\frac{a^2(x-x(t_c))^2}{2}}. \tag{6}$$

For calculating the factors a and b, assuming in the height h_l, the half-width of the profile along the x direction is equal to r_n. Thus, the factor for the initial profile is calculated by solving the following equation,

$$\begin{aligned} &f_0(r_n) = h_l, \\ &\text{s.t.} \int_{-\infty}^{\infty} f_0(x)dx = V_m \Big/ (t_1 - t_0). \end{aligned} \tag{7}$$

With Eq. (7) solved, the profile $f_0(x)$ is fully defined. For the profile $f_0(x)$, typically, its height within the nozzle region χ_n, which is defined as

$$\chi_n = \{x \,||x - x(t_c)| \leqslant r_n\}, \tag{8}$$

is larger than the nozzle height h_l. From time t_c to time $t_c + \delta t$, where δt is the infinitesimal increment of time, the nozzle moves from position $[x(t_c), y(t_c)]^\top$ to position $[x(t_c + \delta t), y(t_c + \delta t)]^\top$, and irons the profile $f_0(x)$ in the nozzle region. Define the profile after the ironing as $f_1(x)$. The proposed OTB-GM method assumes that the ironing effect of the nozzle forces the height in the nozzle region of the profile $f_1(x)$ to satisfy

$$f_1(x) \leqslant h_l, \text{ for } \forall x \in \chi_n. \tag{9}$$

Additionally, since the OTB-GM method simulates the ironing effect of the nozzle, it assumes the presence of a printing base to support the ironing process.

Following the mass conservation, the ironed material within the nozzle region must be relocated. Thus the optimal transport is introduced for solving this relocation processing, resulting in the generation of $f_1(x)$. The generation of the profile $f_1(x)$ from the profile $f_0(x)$ is to find the optimal transport map $\tau(u, v)$, representing the height transported from u to v. The relationship between the profile before and after the transportation for the position v_0 is expressed as

$$f_1(v_0) = f_0(v_0) + \int_{-\infty}^{\infty} \tau(u, v_0)du. \tag{10}$$

The calculation of the transport map $\tau(u, v)$ should consider the solidification process of the MEX. In the MEX, as the fluidity of the printed thermoplastic material is related to its temperature and the material cooling process after leaving the nozzle, the destination range of transportation should be limited. Thus, the OTB-GM method assumes that the reachable region of the extruded material is constrained, and the reachable region of the extruded material is defined as χ_a, with the half-width r_a, i.e.

$$\chi_a = \{x \,||x - x(t_c)| \leqslant r_a\}. \tag{11}$$

The half-width r_a is affected by the layer height h_l, nozzle speed v_n, extrusion speed v_e, and temperature of printing T_p.

As mentioned in the background of the optimal transport, the transport map is generated following the minimum energy consumption principle. In the MEX process, as the material is heated to the semi-molten state by the nozzle [35], the viscous drag during the material flow should be considered. During the ironing process, the height of the relocated material is changed, thus the gravitational potential energy of the profile is added to the model. Additionally, the surface shape of the extruded material after the relocation is modified; thus the surface energy change is taken into account while modeling. Define the viscosity-related energy as ΔE_v, the gravitational-related energy change as ΔE_h, and the surface-related energy change as ΔE_s. The overall transportation energy ΔE is expressed as

$$\Delta E = \Delta E_v + \Delta E_h + \Delta E_s. \tag{12}$$

For the profile $f(x)$, define its material density as ρ_m and the gravitational constant as g; its gravitational potential energy E_h is calculated as

$$E_h = \int_{-\infty}^{\infty} \rho_m g f^2(x)dx. \tag{13}$$

For the transformation process from $f_0(x)$ to $f_1(x)$, the gravitational potential energy change ΔE_h is expressed as

$$\Delta E_h = \mu_h \rho_m g \left(\int_{-\infty}^{\infty} (f_1(x))^2 dx - \int_{-\infty}^{\infty} (f_0(x))^2 dx \right). \tag{14}$$

The factor μ_h in Eq. (14) represents the weight of gravitational potential energy in the OT calculation. The viscosity-related energy is written with respect to the distance between the initial position u and the final position v of the transported material [36–38], i.e.,

$$\Delta E_v = \mu_v \mu_f \rho_m \iint_{-\infty}^{+\infty} (u - v)^2 \tau(u, v)dudv, \tag{15}$$

where μ_v is the factor representing the weight of viscosity-related energy in the profile generation process and μ_f is the material friction coefficient. The surface energy E_s for the profile $f(x)$ is calculated by its surface area S_l and the surface energy coefficient γ_s [39,40], as

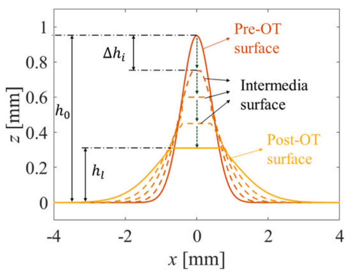

Fig. 4. Step-by-step transportation strategy illustration.

$$E_s = \gamma_s S_l. \tag{16}$$

For the calculation of surface-related energy change ΔE_s, define the height change in the neighborhood for the profile $f(x)$ as $f'(x)$, i.e.,

$$f'(x) = |f(x+\delta x) - f(x)|. \tag{17}$$

The surface-related energy change ΔE_s is thus calculated by combining Eqs. (16) and (17), as

$$\Delta E_s = \mu_s \gamma_m \left(\int_{-\infty}^{\infty} \sqrt{(f_1'(x))^2 + 1}\, dx - \int_{-\infty}^{\infty} \sqrt{(f_0'(x))^2 + 1}\, dx \right), \tag{18}$$

where μ_s is the weight factor of surface-related energy in the OT calculation. The illustration of the energy change during the transportation process is shown in Fig. 3(a). As the energy changes while the transportation process is derived, the proposed method for calculating the transportation map $\tau(u,v)$ is finalized as the following optimization problem,

$$\begin{aligned} &\tau(u,v) = argmin\{\Delta E\}, \\ &\text{s.t. } f_1(x) \leqslant h_l, \text{ for } \forall x \in \chi_n, \\ &\int_{-\infty}^{\infty} f_0(x)dx = \int_{\chi_a} f_1(x)dx. \end{aligned} \tag{19}$$

As the integral equation in this section is involved with infinite upper and lower limits, the practical operation of calculation is as follows. For the profile $f(x)$ involved with the integral, the upper and lower limit for actual calculation is defined as x_l and x_u, respectively. Define a small height δh, and the x_l and x_u is calculated as

$$\begin{aligned} &f(x_l) = \delta h \,(\text{when } \; x_l < x(t_c)), \\ &f(x_u) = \delta h \,(\text{when } \; x_l > x(t_c)). \end{aligned} \tag{20}$$

By solving Eq. (19), the optimal transport map is generated. Based on the transport map, the profile after ironing $f_1(x)$ for the printing process is calculated following Eq. (10). The profile before and after the transportation and the corresponding transport map are illustrated in Fig. 3 (b).

The calculation of Eq. (19) follows the step-by-step distribution strategy, as Fig. 4 shows. Define the profile after the i^{th} distribution as $f_i(x)$, and the transport map from $f_{i-1}(x)$ to $f_i(x)$ is defined as $\tau_i(u,v)$. This step-by-step method generates the profile $f_i(x)$ with the initial condition $f_{i-1}(x)$, helping to reduce the computation time for solving. Define the maximum value of the decreased height in χ_n at each step as Δh_0, and the maximum height at the $f_0(x)$ as h_0. The distribution step d_s is calculated as

$$d_s = \lceil (h_0 - h_l)/\Delta h_0 \rceil. \tag{21}$$

From the first step to the $d_s - 1$ step of distribution, the strategy aims to generate $f_i(x)$ whose maximum height in χ_n is decreased by Δh_0 compared to the previous one $f_{i-1}(x)$. For the final step d_s, the strategy processes the remaining height from the final goal h_l. Define the actual height limitation for the i^{th} step of distribution within χ_n as $h_m^{(i)}$. The $h_m^{(i)}$ is expressed as

$$h_m^{(i)} = \begin{cases} h_0 - i\Delta h_0 \,(\text{when } \; i \leqslant d_s - 1) \\ h_l \,(\text{when } \; i = d_s) \end{cases}. \tag{22}$$

Define the change of energy for each step of the distribution as ΔE_i. The optimization algorithm for each step of distribution is as follows,

$$\begin{aligned} &\tau_i(u,v) = argmin\{\Delta E_i\}, \\ &\text{s.t. } f_i(x) \leqslant h_m^{(i)}, \text{ for } \forall x \in \chi_n, \\ &\int_{\chi_a} f_{i-1}(x)dx = \int_{\chi_a} f_i(x)dx. \end{aligned} \tag{23}$$

3.2. *Material extrusion three-dimensional profile modeling with sequential 3D optimal transport*

Considering the printing situation in 3D (as shown in Fig. 5), the nozzle is moving along the corner trajectory $[x(t), y(t)]^\top$ and the extrusion trajectory is $e(t)$. The nozzle radius of the printer is r_n and the distance between the nozzle and the printing plane is h_l. At a specific time interval $[t^{(k)}, t^{(k+1)}]$, whose middle point is $t_m^{(k)} = (t_{k+1} - t_k)/2$, the nozzle extrudes the material with the volume V_m. Assume the geometry of deposited material $f_d^{(k)}(x,y)$ at the time interval $[t^{(k)}, t^{(k+1)}]$ follows the Gaussian distribution [32–34] after initial extrusion, with the factor a and b. The profile $f_d^{(k)}(x,y)$ is expressed as

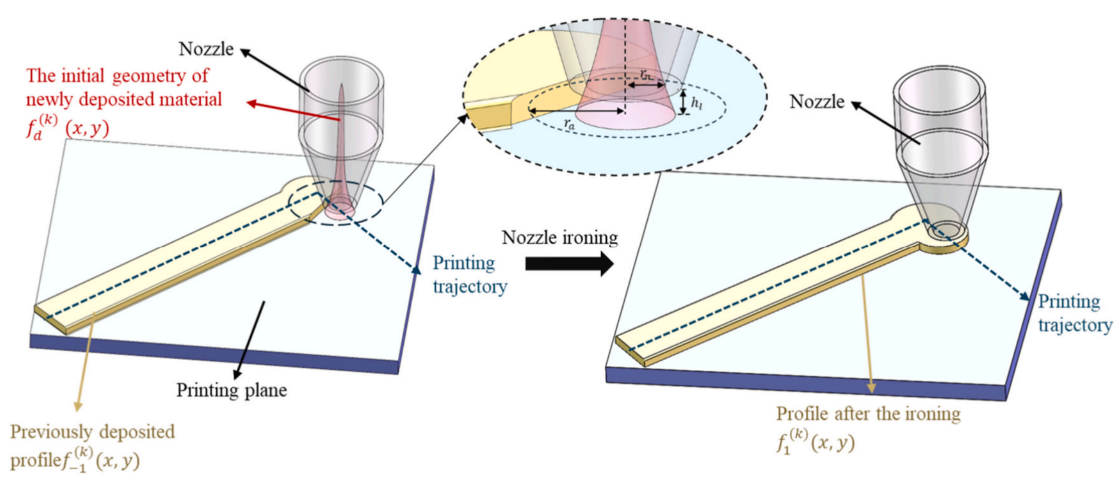

Fig. 5. Illustration of the printing configuration and the profile before and after the transportation in 3D.

$$f_d^{(k)}(x,y) = \frac{b}{2\pi}\exp\left(-\frac{a^2\left(x - x(t_m^{(k)})\right)^2}{2} - \frac{a^2\left(y - y(t_m^{(k)})\right)^2}{2}\right). \tag{24}$$

The factors a and b is determined by the profile height at the edge of nozzle and the deposited volume V_m, i.e.

$$\begin{aligned} & f_d^{(k)}\left(r_n, r_n\right) = h_l, \\ & \text{s.t.} \iint_{x,y} f_d^{(k)}\left(r_n, r_n\right) = V_m. \end{aligned} \tag{25}$$

Assuming that from the start of the printing process to the time $t^{(k)}$, the previously deposited profile is $f_{-1}^{(k)}(x,y)$. The initial height profile $f_0^{(k)}(x,y)$ of the interval $\left[t^{(k)}, t^{(k+1)}\right]$ is the combination of the previously deposited section $f_{-1}^{(k)}(x,y)$ and the newly deposited section $f_d^{(k)}(x,y)$ as Fig. 5 shown, i.e.,

$$f_0^{(k)}(x,y) = f_{-1}^{(k)}(x,y) + f_d^{(k)}(x,y). \tag{26}$$

Similar to the 2D situation, the profile $f_0^{(k)}(x,y)$ is ironed by the moving nozzle, and the printing base existence assumption with respect to the ironing process simulation is also incorporated in the 3D derivation. The optimal transport is employed for solving the profile $f_1^{(k)}(x,y)$, as the result of the nozzle ironing. The transport map from the profile $f_0^{(k)}(x,y)$ to the profile $f_1^{(k)}(x,y)$ is defined as $\tau(u_0, v_0, u_1, v_1)$, representing the height transport from $[u_0, v_0]^\top$ to $[u_1, v_1]^\top$. Thus, the relationship between the two profiles at the point $[u_1, v_1]^\top$ is expressed as

$$f_1^{(k)}(u_1, v_1) = f_0^{(k)}(u_1, v_1) + \iint_{-\infty}^{\infty} \tau(u_0, v_0, u_1, v_1) du_0 dv_0. \tag{27}$$

The determination of the transport map $\tau(u_0, v_0, u_1, v_1)$ follows the transportation energy minimization principle. The energy change during the transportation process is similar to the 2D condition. The equation of energy change is the same as Eq. (12) and the schematic of the transportation process is shown in Fig. 5. For the profile $f(x,y)$, its gravitational potential energy E_h is calculated as

$$E_h = \iint_{-\infty}^{\infty} \rho_m g f^2(x,y) dxdy. \tag{28}$$

Thus, the gravitational potential energy change ΔE_h from the profile $f_0^{(k)}(x,y)$ to $f_1^{(k)}(x,y)$ is calculated as

$$\Delta E_h = \mu_h \rho_m g \left(\iint_{-\infty}^{\infty} \left(f_1^{(k)}(x,y)\right)^2 dxdy - \iint_{-\infty}^{\infty} \left(f_0^{(k)}(x,y)\right)^2 dxdy\right). \tag{29}$$

The energy change associated with viscosity ΔE_v during the transportation process is represented in relation to the distance between the starting position $[u_0, v_0]^\top$ and the final position $[u_1, v_1]^\top$ of the moved material [36–38], i.e.

$$\Delta E_v = \mu_v \mu_f \rho_m \iiiint_{-\infty}^{+\infty} \left|\left|[u_0, v_0]^\top - [u_1, v_1]^\top\right|\right| \tau(u_0, v_0, u_1, v_1) du_1 dv_1 du_0 dv_0 \tag{30}$$

For the surface-related energy part, define the height change in the neighborhood for the profile $f(x,y)$ along the x and y axis as $f_{(x)}{}'(x,y)$ and $f_{(y)}{}'(x,y)$, respectively, i.e.,

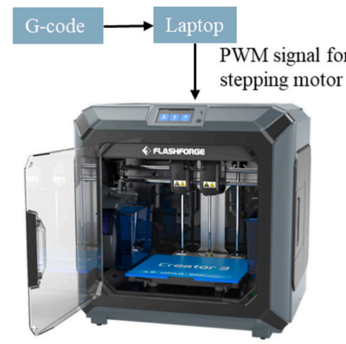

Fig. 6. Experimental Flashforge Creator 3 MEX printer.

$$\begin{aligned} & f_{(x)}{}'\left(x,y\right) = \left|f(x,y) - f(x+\delta x, y)\right|, \\ & f_{(y)}{}'\left(x,y\right) = \left|f(x,y) - f(x, y+\delta y)\right|. \end{aligned} \tag{31}$$

Thus, the surface area S_l for the profile $f(x,y)$ is expressed as

$$S_l = \sqrt{\left(f_{(x)}{}'\right)^2 + \left(f_{(y)}{}'\right)^2 + 1}. \tag{32}$$

By combining the Eqs. (16) and (32), the energy change caused by the surface ΔE_s [39,40] is written as

$$\Delta E_s = \mu_s \gamma_m \left(\iint_{-\infty}^{\infty} \sqrt{\left(f^{(k)}{}_{1(x)}{}'\right)^2 + \left(f^{(k)}{}_{1(y)}{}'\right)^2 + 1} - \sqrt{\left(f^{(k)}{}_{0(x)}{}'\right)^2 + \left(f^{(k)}{}_{0(y)}{}'\right)^2 + 1}\right) dxdy, \tag{33}$$

The solution of the transport map $\tau(u_1, v_1, u_0, v_0)$ should consider the cooling process of the material and the nozzle position constraint, similar to the situation in the 2D condition. Define the nozzle region χ_n as

$$\chi_n = \left\{(x,y) \,\middle|\, \left|x - x(t_m^{(k)}), y - y(t_m^{(k)})\right|_2 \leqslant r_n\right\}. \tag{34}$$

Due to the nozzle position constraint, the OTB-GM method assumes that the profile $f_1^{(k)}(x,y)$ in the nozzle region must be lower than the nozzle height, i.e.,

$$f_1^{(k)}\left(x,y\right) \leqslant h_l, \text{ for } \forall\left(x,y\right) \in \chi_n. \tag{35}$$

Considering the forming process is involved with material cooling (as the temperature of the printed material decreases after it leaves the nozzle), the OTB-GM method assumes a constrained reachable region of the printed material. Define the material reachable region as χ_a. The radius of χ_a is r_a, and the χ_a is thus defined as,

$$\chi_a = \left\{(x,y) \,\middle|\, \left|x - x(t_m^{(k)}), y - y(t_m^{(k)})\right|_2 \leqslant r_a\right\}. \tag{36}$$

The radius r_a is related to the layer height h_l, nozzle speed v_n, extrusion speed v_e and temperature of printing T_p.

In summary, the proposed method for transport map calculation in 3D is as the following equation,

Table 1
Printing parameters of the Flashforge Creator 3.

Printer maximum size	300 × 250 × 200 mm^3
Printer name	Flashforge Creator 3
Nozzle diameter	0.4 mm
Acceleration	500 mm/s^2
Corner trajectory blending tolerance	0.05 mm
Printing material	PLA
Thermal expansion coefficient	41 μm/(m·K)
Nozzle temperature	230 °C
Print bed temperature	60 °C
Nozzle speed	30 mm/s

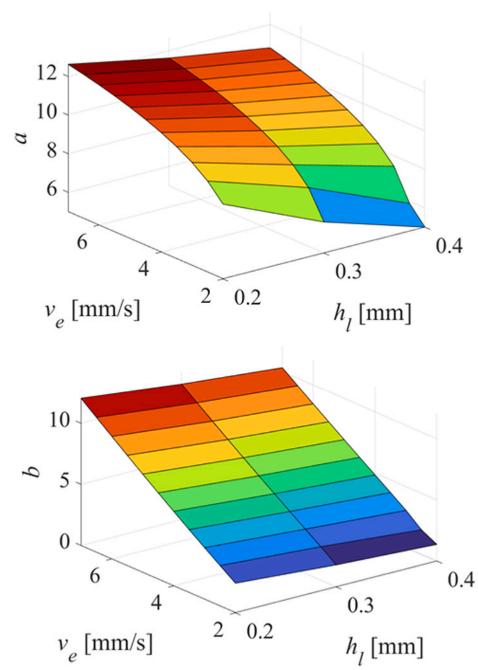

Fig. 7. The illustration of the calculated factor of the line printing experiment.

$$\begin{aligned} &\tau(u_1, v_1, u_0, v_0) = \operatorname{argmin}\{\Delta E\}, \\ &\text{s.t. } f_1^{(k)}\left(x, y\right) \leqslant h_l, \text{ for } \forall \left(x, y\right) \in \chi_n, \\ &\iint_{-\infty}^{\infty} f_0^{(k)}\left(x, y\right) dxdy = \iint_{\chi_a} f_1^{(k)}\left(x, y\right) dxdy. \end{aligned} \tag{37}$$

The result of Eq. (37) provides the optimal transport map between two profiles. Following Eq. (27), the profile after the nozzle ironing $f_1^{(k)}(x,y)$ is calculated. The illustration of the initial profile $f_0^{(k)}(x,y)$, the final profile $f_1^{(k)}(x,y)$, and the corresponding transport map in the representative positions is shown in Fig. 5(c). After solving the transportation at the interval $\left[t^{(k)}, t^{(k+1)}\right]$, its distribution result $f_1^{(k)}(x,y)$ is set as the previously deposited material profile $f_{-1}^{(k+1)}(x,y)$ at the interval $\left[t^{(k+1)}, t^{(k+2)}\right]$. This transportation calculation process is sequentially executed in the interval $\left[t^{(k)}, t^{(k+1)}\right]$, $\left[t^{(k+1)}, t^{(k+2)}\right]$, $\left[t^{(k+2)}, t^{(k+3)}\right]$,$\cdots$, until the end of the printing process. By the sequential simulating strategy, the distribution result in the final interval of printing trajectory is generated, as the overall deposited profile.

4. Experiment verification of proposed OTB-GM method

4.1. Experimental platform and simulation parameters setup

The verification platform is Flashforge Creator 3 MEX printer, as shown in Fig. 6. To accurately control the nozzle and extrusion trajectory, the control laptop generates the pulse width modulation (PWM) single from the input G-code and sends the PWM signal to the stepping motors of the printer. The specifications of the printer are shown in Table 1.

While simulating the extrusion profile, the factor μ_v, μ_g, and μ_s are set equally as 1, and the radius of the nozzle r_n is set as 0.2 mm. The mesh size p for simulation is 0.1 mm. The radius of the material available region r_a is decided by experiment. Based on the experiment, the radius r_a increases with the decreasing of layer height h_l, nozzle speed v_n, and the increasing of extrusion speed v_n. The factors of the Gaussian distribution in Eq. (6) of the initial profile are shown in Fig. 7.

4.2. Experiment verification of the 2D OTB-GM method

The lines are printed to verify the proposed 2D OTB-GM method. The designed verification line part includes the printed trajectory under different extrusion speeds v_e (as Fig. 8 (a) shows), and the trajectory is printed under a series of layer heights h_l. The printed line parts are cut with a plane perpendicular to the printing trajectory, and the corresponding simulation result is calculated by the 2D simulation method. The extrusion profile according to the slice image of the actual printed part is extracted. Define the point set of the image-extracted profile and the simulated profile by the OTB-GM method as $(x_i, z_i) \in \boldsymbol{P}_i$ and $(x_s, z_s) \in \boldsymbol{P}_s$, respectively. To align the two profiles, the image-extracted profile $\boldsymbol{P}_i$ is moved with distance Δd_x and Δd_z along the x and z axis, respectively. The calculation of Δd_x and Δd_z is processed by minimizing the distance between two profiles after moving, i.e.,

$$(\Delta d_x, \Delta d_z) = \operatorname{argmin} \sum_{(x_i, z_i) \in \boldsymbol{P}_i} \min_{(x_s, z_s) \in \boldsymbol{P}_s} |(x_i + \Delta d_x, z_i + \Delta d_z) - (x_s, z_s)|_2. \tag{38}$$

With the moving distance calculated, the aligned image-extracted profile $\left(x_i{}^{(a)}, z_i{}^{(a)}\right) \in \boldsymbol{P}_i{}^{(a)}$ is calculated. The slice image of the actual printed line, the corresponding aligned image-extracted profile $\boldsymbol{P}_i{}^{(a)}$, and the corresponding simulated profile from the OTB-GM method $\boldsymbol{P}_s$ are shown in Fig. 9. The conventional ellipse geometry modeling profile $\boldsymbol{P}_e$

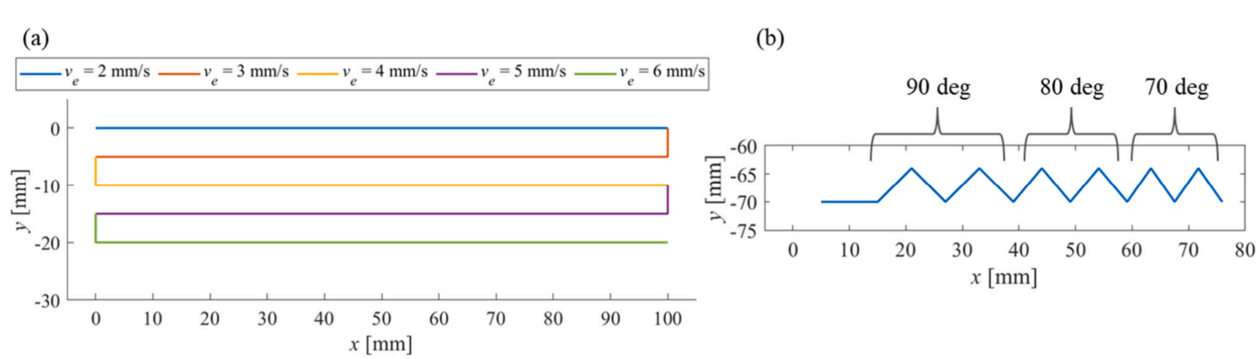

Fig. 8. (a) The trajectory illustration of line verification parts, and (b) the corner verification parts.

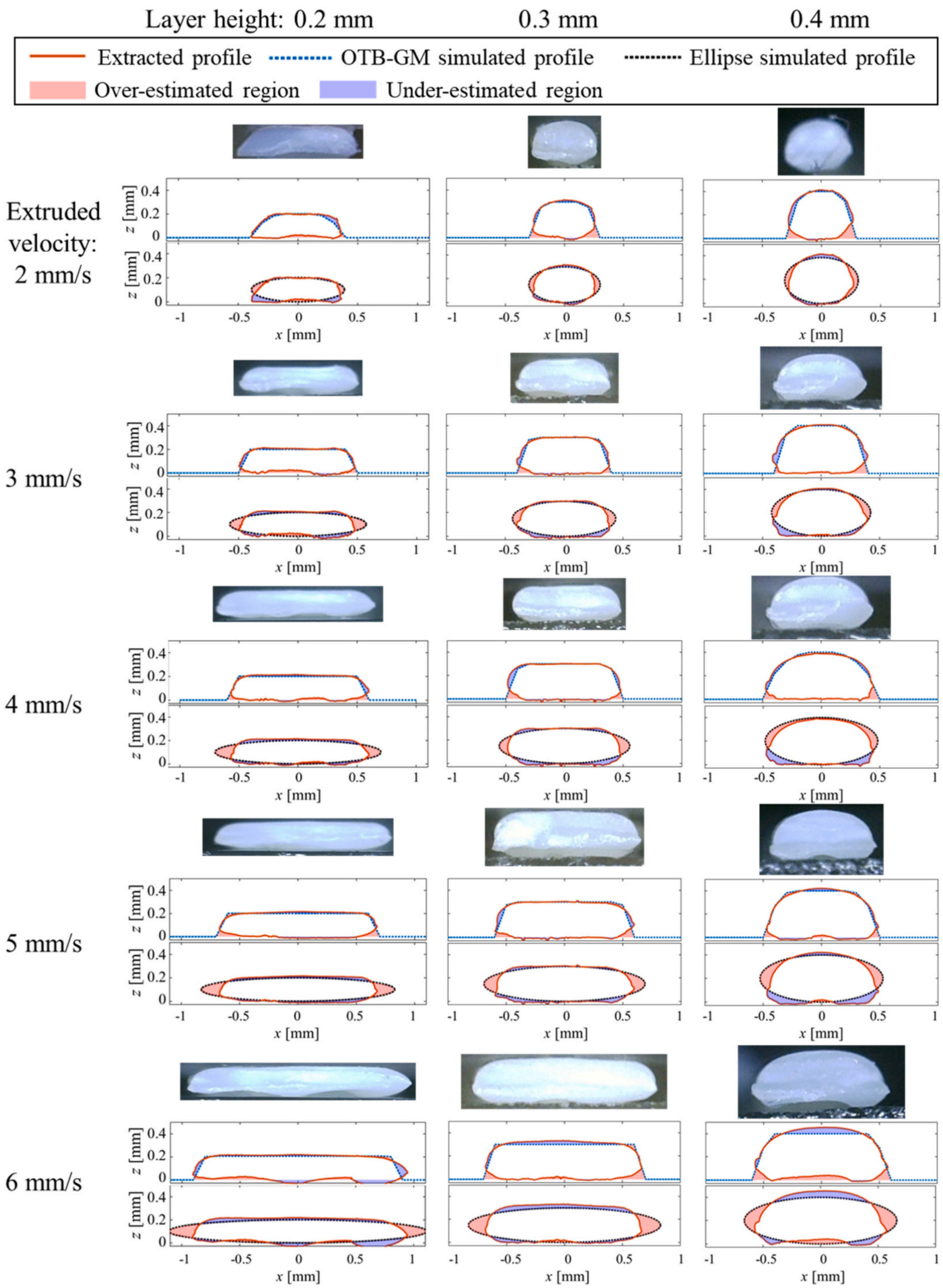

Fig. 9. The comparison of the extruded geometry of the actual printed line part, the proposed OTB-GM method, and the ellipse modeling method [9].

is also illustrated in Fig. 9. The transport map for the OTB-GM simulated profile of the line parts is shown in Fig. 10.

For the cross-section profile of the line part shown in Fig. 9, the left and right halves of the profile exhibit symmetry. For the profile simulated at the specified layer height $h_l = 0.4$mm, there is a flat top region near the nozzle center (i.e., in position $x = 0$). Outside the flat region, the height of the profile decreases as the distance from the nozzle center increases. The explanation for the simulated profile is as follows. Due to viscous resistance during material flow, the material tends to stay in place without moving; and based on the profile before transportation, the material is inclined to concentrate in the region near the nozzle center after the transportation process. Considering the concentration effect of the material and the constraint of nozzle height h_l jointly, the profile height in the nozzle region χ_n is generated as h_l. When moving out of the nozzle region, although the maximum height constraint is no longer applied, the flat region continues. That is mainly because the gravitational potential energy and surface energy minimization strategy overtake the viscous resistance energy consumption minimization in this part of the profile. The surface energy is minimized while the profile height remains constant with position x changing, and the gravitational potential energy minimization prevents the profile from bulging compared with the nozzle region χ_n. Moving beyond the flat region, the gravity-related part of the proposed modeling method is dominant. For some parts of the material in this region, the force to reduce the

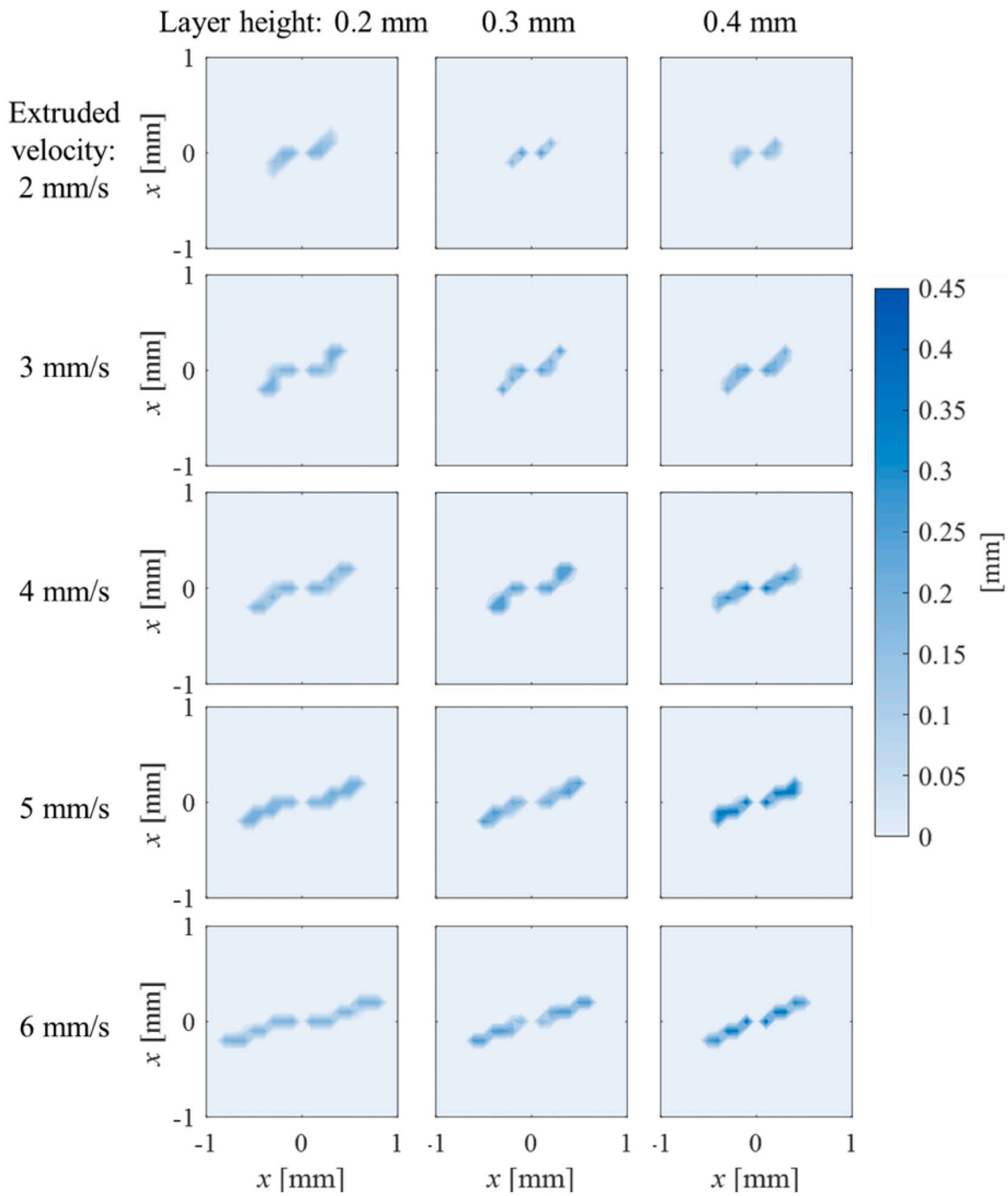

Fig. 10. The transport map of the line part by the proposed OTB-GM method.

gravitational potential energy outweighs the energy consumption of the material flow. Thus this part of extruded material is transported to the position that is further away from the nozzle center but with lower height. The simulated profiles with height $h_l = 0.3$ mm present a similar feature, excluding the profile printed with extrusion speed $v_e = 6$ mm/s. In that case, the simulated profile does not show a region of gradually decreasing height, but have a rectangular shape. This phenomenon indicates that while the extrusion speed remains constant, decreasing the nozzle height cannot expand the material available region χ_a significantly, and that causes the material to fulfill the χ_a region with constant height at h_l considering the mass conservation. The rectangular shape under the low nozzle height-extrusion ratio (i.e., h_l/v_e ratio) appears for most cases printed under $h_l = 0.2$ mm. While the nozzle height-extrusion ratio is increased (for the case printed at $v_e = 2$ mm/s and $h_l = 0.2$ mm), the gradually decreasing height region is observed.

For evaluation of the performance of the proposed OTB-GM modeling methods, the area of over- and under-estimated region area for each case (A_o and A_u, respectively) is calculated, as shown in Fig. 9. The overall estimation deviation area A_d is calculated as

$$A_d = A_o + A_u. \tag{39}$$

The average estimation deviation area A_d of the line parts printed under a series of experiment extrusion speeds, as determined by the OTB-GM and the standard ellipse method respectively, is shown in Fig. 11(a). Compared with the ellipse modeling method, the proposed OTB-GM method reduces the estimation deviation area A_d significantly. As

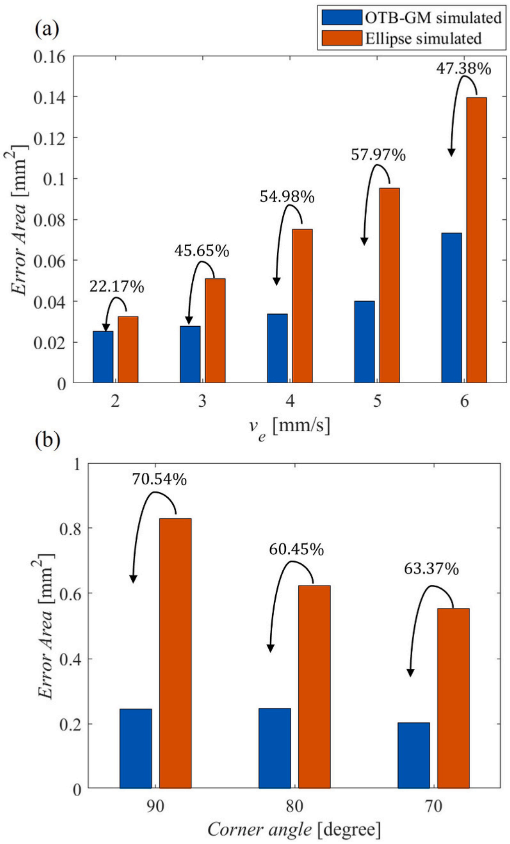

Fig. 11. The comparison of the deviation area of the proposed OTB-GM simulated results that of the ellipse method [9] of (a) 2D case, and (b) 3D case.

illustrated in Fig. 9, the ellipse simulation method significantly over-estimates the left and right edges of the cross-section compared with the OTB-GM method. For the cases with a high h_l/v_e ratio, the simulation profile by the proposed OTB-GM method more accurately reflects the height descending phenomenon from the nozzle center to the sides, helping to improve the estimation accuracy.

4.3. Experiment verification of the 3D OTB-GM method

The corner parts are printed to verify the 3D derivation of the proposed OTB-GM method. The corner trajectory includes a series of corner shapes (as Fig. 8(b) shows), and it is printed under various extrusion speeds v_e, while the layer height h_l is fixed at 0.3 mm. The boundary of the actual printed corner part in the xy plane is extracted as $\boldsymbol{P}_i$, and that of OTB-GM method $\boldsymbol{P}_s$ is generated by the contour of OTB-GM calculated profile, with the level $l_t = 0.02$mm. The $\boldsymbol{P}_i$ is moved and aligned with $\boldsymbol{P}_s$, following the strategy shown in Eq. (38). The image of printed corners, the corresponding aligned actual extrusion profile $\boldsymbol{P}_i{}^{(a)}$, and the OTB-GM method profile $\boldsymbol{P}_s$ are illustrated in Fig. 12. The conventional ellipse geometry modeling profile $\boldsymbol{P}_e$ is also illustrated in Fig. 12. The illustration of the transportation processing at the representative sampling time for the 90-degree corner with the extrusion speed of 5.5 mm/s is shown in Fig. 13.

To evaluate the capability of the proposed OTB-GM model in simulating the extrusion inaccuracy in the corner region, we extract the extrusion inaccuracy region following the method in [41]. In this region, the under-estimated region A_o and the over-estimated region A_u are extracted, as shown in Fig. 12. Following Eq. (39), the average estimation deviation area A_d for a series of corners printed under different extrusion speeds, as determined by both the OTB-GM method and standard ellipse method, is illustrated in Fig. 11(b). In the standard ellipse method's simulated results for most cases, an over-estimation issue is observed in the outer region near the corner center, while under-estimation occurs in the entering and exiting corner regions. Compared with the ellipse method, the estimation results from the proposed OTB-GM modeling effectively eliminate these problems.

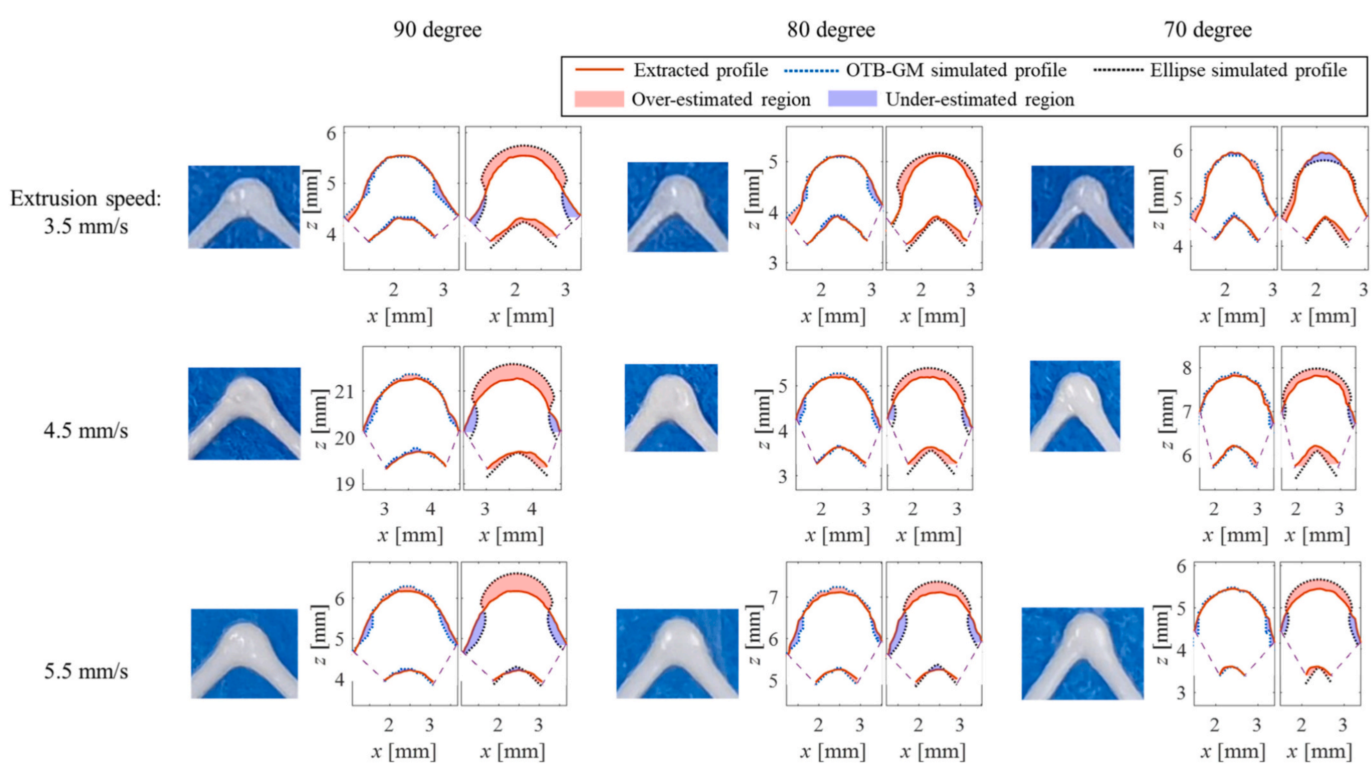

Fig. 12. The comparison of the extruded geometry of the actual printed corner part, the ellipse modeling method [9], and the proposed OTB-GM method.

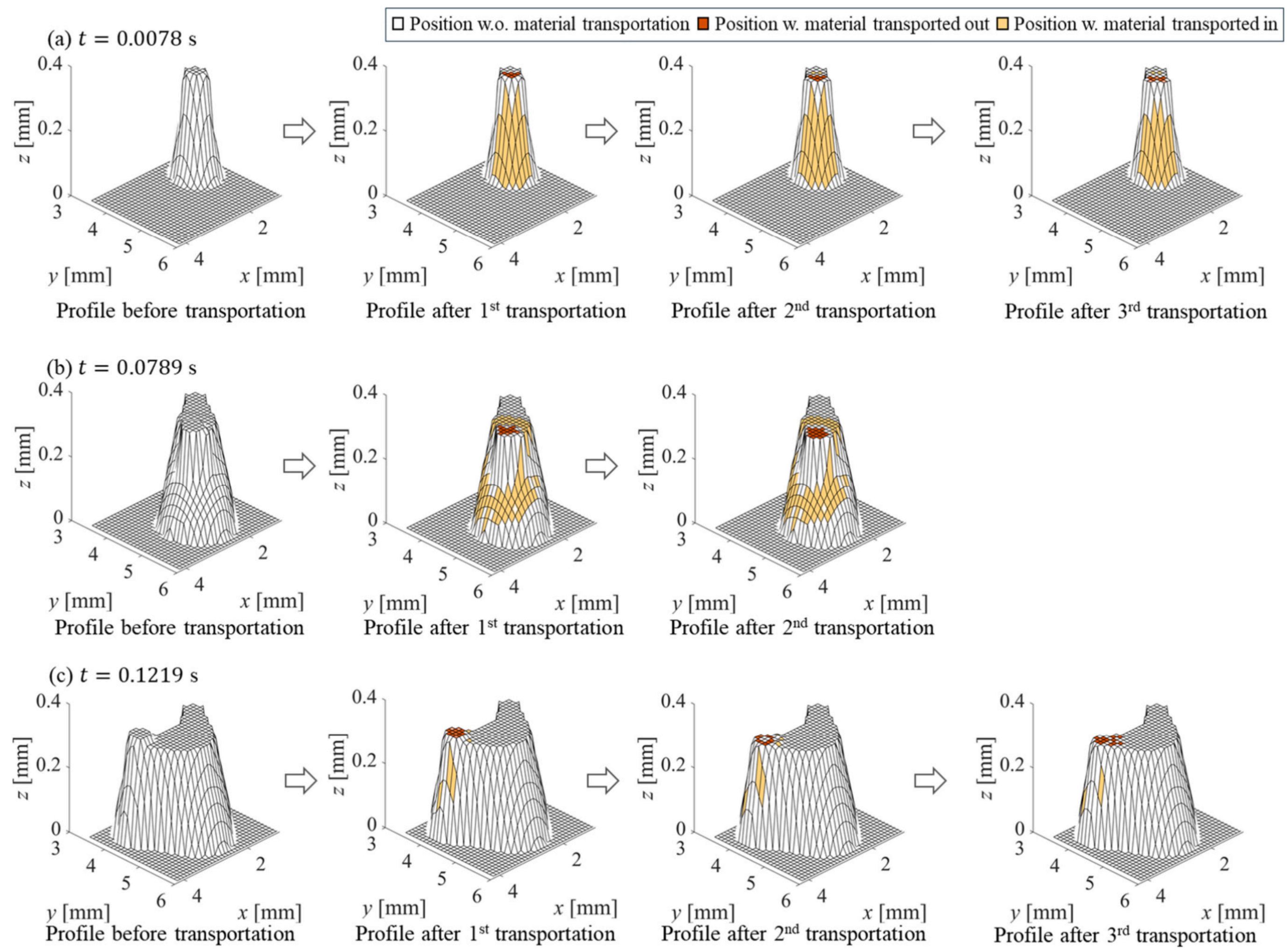

Fig. 13. The illustration of the transportation processing for the 90-degree corner.

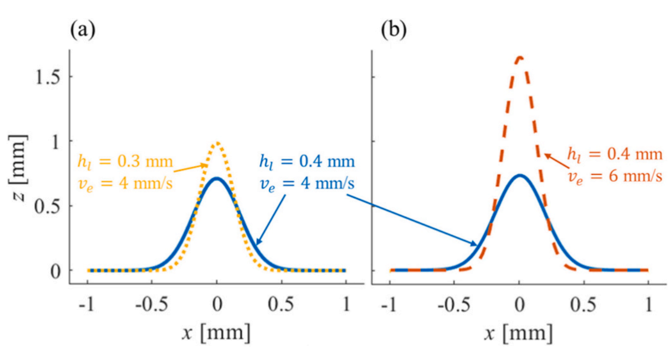

Fig. 14. The illustration of the sensitivity for the profile before transportation with respect to (a) layer height and (b) extrusion velocity.

4.4. The processing parameters sensitivity analysis of the proposed OTB-GM method

The experiment verification of the proposed OTB-GM method involves the change of layer height h_l, extrusion velocity v_e (both in 2D verification), and the nozzle speed v_n (in 3D verification). The sensitivity of the proposed OTB-GM method to the printing process parameters is analyzed from two perspectives: the profile before transportationf_0 and the profile after transportation f_1.

In the OTB-GM method, the profile before transportation f_0 is mainly affected by the layer height h_l and extrusion velocity v_e of printing. Define the sensitivity factor of the profile f_0 for the layer height h_l and extrusion velocity v_e as $\epsilon_h^{(b)}$ and $\epsilon_e^{(b)}$, respectively, which are calculated as

$$\epsilon_e^{(b)} = \frac{\partial f_0}{\partial v_e},$$
$$\epsilon_h^{(b)} = \frac{\partial f_0}{\partial h_l}. \tag{40}$$

The effect of layer height h_l on the profile f_0 is illustrated in Fig. 14(a). The blue solid profile illustrates the profile f_0 with layer height $h_l = 0.4$ mm, and that of the yellow dashed profile is $h_l = 0.3$ mm, and the extrusion velocity v_e for both of them are 4 mm/s. With the layer height decreasing, the entire curve exhibits an increased height and reduced width. Fig. 14(b) illustrates the changes that occur when the extrusion speed v_e is varied. The layer heights h_l for the cases in Fig. 14(b) are both 0.4 mm, and the extrusion speeds for the blue solid profile and red dashed profile are 4 mm/s and 6 mm/s, respectively. Compared to the blue solid profile, the red dashed profile exhibits greater height in the nozzle region due to the increased volume of the extruded material. Additionally, to maintain the profile height constrained at the edge of the nozzle, as shown in Eqs. (7) and (25), the profile height outside the nozzle region is reduced.

For the profile after transportation f_1, define its sensitivity factor for layer height h_l, extrusion velocity v_e, and the nozzle speed v_n as $\epsilon_h^{(a)}$, $\epsilon_e^{(a)}$, and $\epsilon_n^{(a)}$, respectively, which are calculated as

$$\epsilon_e^{(a)} = \frac{\partial f_1}{\partial v_e}, \quad \epsilon_h^{(a)} = \frac{\partial f_1}{\partial h_l}, \quad \epsilon_n^{(a)} = \frac{\partial f_1}{\partial v_n}. \tag{41}$$

The processing parameters affect the profile f_1 by affecting the radius r_a of the material reachable region χ_a. In the 2D verification, the extrusion speed and nozzle height are changed. As the extrusion speed v_n increases, more material is extruded per unit time, resulting in a slower temperature decrease and solidification process. Consequently, the material reachable region χ_a is expanded, and the extruded material is transported further from the nozzle. This is supported by the comparison of the transportation map in the column of Fig. 10. As the nozzle height h_l decreases, the pressure exerted by the nozzle on the extruded material increases, resulting in enhanced fluidity of the extruded material and an expanded reachable region. This observation is corroborated by the comparison of the transportation map in row of Fig. 10. The effect of nozzle speed v_n is shown in the 3D verification case. In the corner region, the radius r_a of the material reachable area increment is observed as the nozzle speed v_n decreases, as Fig. 12 shows. This phenomenon can be explained as follows: a decrease in nozzle speed results in more material being extruded in a given area, which in turn slows down the temperature decrease and solidification process, thereby enlarging the material's reachable region.

5. Conclusions

This paper proposed an optimal-transport-based geometry modeling (OTB-GM) method for material extrusion (MEX) additive manufacturing. The OTB-GM model simulates the ironing effects of the moving nozzle. By calculating the transport map of the flowable printed material, which is caused by the nozzle movement, the OTB-GM generates the final extruded profile. The OTB-GM starts with an initial profile that resembles a Gaussian distribution before ironing. In developing the model, we consider the energy consumption caused by the material's viscous resistance, variations in gravitational potential energy, and changes to the surface geometry that occur during the ironing process. The calculation of the printed material's transportation map follows the minimal energy-consuming assumption. The proposed OTB-GM method includes the profile generation method in both 2-dimensional (2D), for steady extrusion situations, and in 3-dimensional (3D), for dynamic extrusion conditions. The proposed OTB-GM method is validated by printing line parts and corner parts, for 2D and 3D modeling verification, respectively. The printed result shows that compared with the conventional ellipse geometry modeling method, the proposed OTB-GM method reaches higher accuracy in predicting extruded material geometry. The experiment result shows that the proposed OTB-GM method is capable of modeling the bead geometry of the MEX method with low complexity and computation load, providing the potential of utilizing the OTB-GM method for real-time geometry prediction and printing parameter optimization.

The proposed OTB-GM method is capable of modeling the bead geometry of the MEX method with low complexity and computation load, as well as not relying on a large amount of high-precision measurement data. These features of the proposed OTB-GM provide the potential of utilizing the OTB-GM method for real-time geometry prediction and printing parameter optimization. The OTB-GM model has several potential applications in industrial settings. The OTB-GM can be utilized for in-situ process monitoring and control, allowing for the immediate adjustment of printing parameters to ensure that the final product meets design specifications, thereby reducing waste, enhancing production efficiency, and improving the sustainability of manufacturing. The OTB-GM method's ability to predict geometry allows manufacturers to estimate the dimensions of printed parts, potentially replacing some functions traditionally performed by measurement equipment and thereby helping to reduce manufacturing costs. Additionally, as the OTB-GM method is capable of providing the printing result under given printing parameters, it can assist the manufacturer to find the optimal printing parameters with satisfied dimensional accuracy, thus reducing the waste rate in production and improving the sustainability.

While applying the current OTB-GM method in geometric modeling, it is important to recognize some limitations of this approach. The proposed OTB-GM method is specifically designed to account for the nozzle ironing effect, making it primarily applicable to the MEX method. This approach is involved with the temperature decrease and solidification process of the extruded material as it exits the nozzle, which restricts the printed materials to thermoplastics. Furthermore, the OTB-GM method does not take thermal expansion into account, requiring that the coefficient of thermal expansion for the printed material be sufficiently small to ensure accuracy. Additionally, the method assumes the presence of a printing base that provides the necessary support for the ironing process; thus, it does not consider the extruded profile under roofing and bridging printing conditions. Based on the limitations mentioned above, the OTB-GM method can be improved by taking thermal shrinkage into account and considering solidification conditions beyond just thermal plastic materials, thereby expanding the applicable range of printing materials covered.

CRediT authorship contribution statement

Siqi Chen: Writing – review & editing, Writing – original draft, Visualization, Validation, Software, Methodology, Investigation, Formal analysis, Data curation, Conceptualization. **Shuai Liu:** Visualization, Validation, Software, Resources. **Shuaiyin He:** Visualization, Validation. **Molong Duan:** Writing – review & editing, Writing – original draft, Visualization, Supervision, Resources, Project administration, Methodology, Funding acquisition, Formal analysis, Data curation, Conceptualization.

Declaration of Generative AI and AI-assisted technologies in the writing process

The writing process only uses ChatGPT and Grammarly AI to perform grammar checks.

Declaration of competing interest

The authors declare that they have no known competing financial interests or personal relationships that could have appeared to influence the work reported in this paper.

Acknowledgment

The authors acknowledge support from the Research Grants Council (RGC) of the Government of Hong Kong Special Administrative Region (HKSAR) with RGC/ECS Project (No. 26215824), the Frontier Technology Research for Joint Institutes with industry scheme under grant OKT24EG07, The Innovation and Technology Commission's ITF - Guangdong-Hong Kong Technology Cooperation Funding Scheme (Platform Research Scheme) with number GHP/170/22SZ, as well as the HKUST – HKUST(GZ) Cross-campus Collaborative Research Scheme under the Great Bay Area "1+1+1" Joint Funding Program. This work was supported in part by the Project of Hetao Shenzhen-Hong Kong Science and Technology Innovation Cooperation Zone (HZQB-KCZYB-2020083). The help from the funding agency and the other researchers is sincerely appreciated.

Appendix A. Supplementary data

Supplementary data to this article can be found online at https://doi.org/10.1016/j.jmapro.2025.09.042.

References

[1] Wong KV, Hernandez A. A review of additive manufacturing. ISRN Mech Eng 2012; 2012:1–10. https://doi.org/10.5402/2012/208760.

[2] Bikas H, Stavropoulos P, Chryssolouris G. Additive manufacturing methods and modeling approaches: a critical review. Int J Adv Manuf Technol 2016;83: 389–405. https://doi.org/10.1007/s00170-015-7576-2.

[3] Lhachemi H, Malik A, Shorten R. Augmented reality, cyber-physical systems, and feedback control for additive manufacturing: a review. IEEE Access 2019;7: 50119–35. https://doi.org/10.1109/ACCESS.2019.2907287.

[4] Everton SK, Hirsch M, Stavroulakis PI, Leach RK, Clare AT. Review of in-situ process monitoring and in-situ metrology for metal additive manufacturing. Mater Des 2016;95:431–45. https://doi.org/10.1016/j.matdes.2016.01.099.

[5] Kechagias JD. Surface roughness assessment of ABS and PLA filament 3D printing parts: structural parameters experimentation and semi - empirical modelling. Int J Adv Manuf Technol 2024:1935–46. https://doi.org/10.1007/s00170-024-14232-0.

[6] Kechagias JD, Fountas NA, Papantoniou I, Vaxevanidis NM. Interlaminar bonding assessment in vertical - oriented filament material extrusion bending specimens. Int J Adv Manuf Technol 2025:4977–89. https://doi.org/10.1007/s00170-025-15124-7.

[7] Kumar P, Patel R, Singh I, Agrawal S, Kechagias JD. Optimising the fused filament fabrication process employing the experimental design approach: an expository paradigm under cold weather conditions and lightweight specimens. Next Mater 2025;7:100387. https://doi.org/10.1016/j.nxmate.2024.100387.

[8] Comminal R, Serdeczny MP, Pedersen DB, Spangenberg J. Motion planning and numerical simulation of material deposition at corners in extrusion additive manufacturing. Addit Manuf 2019;29:100753. https://doi.org/10.1016/j.addma.2019.06.005.

[9] Wang P, Zou B, Ding S. Modeling of surface roughness based on heat transfer considering diffusion among deposition filaments for FDM 3D printing heat-resistant resin. Appl Therm Eng 2019;161:114064. https://doi.org/10.1016/j.applthermaleng.2019.114064.

[10] Serdeczny MP, Comminal R, Pedersen DB, Spangenberg J. Experimental validation of a numerical model for the strand shape in material extrusion additive manufacturing. Addit Manuf 2018;24:145–53. https://doi.org/10.1016/j.addma.2018.09.022.

[11] Huang Q, Member S, Wang Y, Lyu M, Lin W. Shape deviation generator — a convolution framework for learning and predicting 3-D printing shape accuracy. IEEE Trans Autom Sci Eng 2020;17:1486–500. https://doi.org/10.1109/TASE.2019.2959211.

[12] Haghbin N, Bone D, Young K. Controlled extrusion-based 3D printing of micro-channels with the geometric modelling of deposited roads. J Manuf Process 2021; 67:406–17. https://doi.org/10.1016/j.jmapro.2021.04.067.

[13] Ullah AMMS. Geometric modeling and 3D printing using recursively generated point cloud. 2019.

[14] Sutjipto S, Tish D, Paul G, Vidal-Calleja T, Schork T. Towards visual feedback loops for robot-controlled additive manufacturing. Robot Fabr Archit Art Des 2018;2019: 85–97. https://doi.org/10.1007/978-3-319-92294-2_7.

[15] Nuchitprasitchai S, Roggemann M, Pearce JM. Factors effecting real-time optical monitoring of fused filament 3D printing. Prog Addit Manuf 2017;2:133–49. https://doi.org/10.1007/s40964-017-0027-x.

[16] Friedrich L, Begley M. In situ characterization of low-viscosity direct ink writing: stability, wetting, and rotational flows. J Colloid Interface Sci 2018;529:599–609. https://doi.org/10.1016/j.jcis.2018.05.110.

[17] Ferraris E, Zhang J, Van Hooreweder B. CIRP annals - manufacturing technology thermography based in-process monitoring of fused filament fabrication of polymeric parts. CIRP Ann - Manuf Technol 2019;68:213–6. https://doi.org/10.1016/j.cirp.2019.04.123.

[18] Borish M, Post BK, Roschli A, Chesser PC, Love LJ, Borish M, et al. ScienceDirect ScienceDirect real-time defect correction in large-scale polymer additive real-time defect correction in large-scale polymer additive manufacturing via thermal imaging and laser profilometer manufacturing via thermal imaging and laser profil. Procedia Manuf 2020;48:625–33. https://doi.org/10.1016/j.promfg.2020.05.091.

[19] Borish M, Post BK, Roschli A, Chesser PC, Love LJ, Gaul KT. Defect identification and mitigation via visual inspection in large-scale additive manufacturing. JOM 2019;71:893–9. https://doi.org/10.1007/s11837-018-3220-6.

[20] Gao Y, Li B, Wang WEI, Xu W, Zhou CHI, Jin Z. Watching and safeguarding your 3D printer: online process monitoring against cyber-physical attacks2; 2018. https://doi.org/10.1145/3264918.

[21] Li L, McGuan R, Isaac R, Kavehpour P, Candler R. Improving precision of material extrusion 3D printing by in-situ monitoring & predicting 3D geometric deviation using conditional adversarial networks. Addit Manuf 2021;38:101695. https://doi.org/10.1016/j.addma.2020.101695.

[22] Sharma P, Vaid H, Vajpeyi R, Shubham P, Agarwal KM, Bhatia D. Predicting the dimensional variation of geometries produced through FDM 3D printing employing supervised machine learning. Sensors Int 2022;3:100194. https://doi.org/10.1016/j.sintl.2022.100194.

[23] Charalampous P, Kostavelis I, Kontodina T, Tzovaras D. Learning-based error modeling in FDM 3D printing process. Rapid Prototyp J 2021;(3):507–17. https://doi.org/10.1108/RPJ-03-2020-0046.

[24] Ntousia M, Fudos I, Moschopoulos S, Stamati V. Predicting geometric errors and failures in additive manufacturing. Rapid Prototyping J 2023;(9):1843–61. https://doi.org/10.1108/RPJ-11-2022-0402.

[25] Wang Y, Huang J, Wang Y, Feng S, Peng T, Yang H, et al. A CNN-based adaptive surface monitoring system for fused deposition modeling. IEEE/ASME Trans Mechatron 2020;25:2287–96. https://doi.org/10.1109/TMECH.2020.2996223.

[26] Wang Y, Lin Y, Zhong RY, Xu X. IoT-enabled cloud-based additive manufacturing platform to support rapid product development. Int J Prod Res 2019;57:3975–91. https://doi.org/10.1080/00207543.2018.1516905.

[27] Becker P, Roth C, Roennau A, Dillmann R. Acoustic anomaly detection in additive manufacturing with long short-term memory. Neural Netw 2020:921–6.

[28] Li Z, Zhang Z, Shi J, Wu D. Prediction of surface roughness in extrusion-based additive manufacturing with machine learning. Robot Comput Integr Manuf 2019; 57:488–95. https://doi.org/10.1016/j.rcim.2019.01.004.

[29] Schlegel P, Briele K, Schmitt RH. Autonomous data-driven quality control in self-learning production systems: Proceedings of the 8th Congress of the German Academic Autonomous data-driven quality control in self-learning production systems. 2019. https://doi.org/10.1007/978-3-030-03451-1.

[30] Zhu Z, Anwer N, Mathieu L, Guo K, Qiao L. ScienceDirect convolutional neural network for geometric deviation prediction in additive manufacturing 2023;91: 534–9. https://doi.org/10.1016/j.procir.2020.03.108.

[31] Peyré G, Cuturi M. Computational optimal transport 2019;11. https://doi.org/10.1561/2200000073.

[32] Eagar TW, Tsai NS. Temperature fields produced by traveling distributed heat sources. Weld J (Miami, Fla) 1983;62:346–55.

[33] Ertay DS, Vlasea M, Erkorkmaz K. Thermomechanical and geometry model for directed energy deposition with 2D / 3D toolpaths. Addit Manuf 2020;35:101294. https://doi.org/10.1016/j.addma.2020.101294.

[34] Goodwin J, Flamm J, Narayanan B, Saleeby K, Tucker T, Saldaña C. Digital bead modeling for wire-arc directed energy deposition. J Manuf Process 2024;129: 109–21. https://doi.org/10.1016/j.jmapro.2024.08.060.

[35] Oleff A, Küster B, Stonis M, Overmeyer L. Process monitoring for material extrusion additive manufacturing: a state - of - the - art review. Prog Addit Manuf 2021;6: 705–30. https://doi.org/10.1007/s40964-021-00192-4.

[36] Mahajan SP. Shear Viscosity of Clays to Compute Viscous Resistance. 2008. p. 1–6.

[37] Mizerovskiy LN, Smirnov PR. Viscosity and internal friction in liquids. Russ J Gen Chem 2021;91:1797–806. https://doi.org/10.1134/S1070363221090279.

[38] Peng J, Feng R, Xue M, Zhou E, Wang J, Zhong Z, et al. Research progress and engineering applications of viscous fluid mechanics. 2025. p. 1–27.

[39] Egry I, Ricci E, Novakovic R, Ozawa S. Surface tension of liquid metals and alloys — recent developments. Adv Colloid Interface Sci 2010;159:198–212. https://doi.org/10.1016/j.cis.2010.06.009.

[40] Packham DE. Surface energy , surface topography and adhesion. Int J Adhes Adhes 2003;23:437–48. https://doi.org/10.1016/S0143-7496(03)00068-X.

[41] Chen S, Yang Y, Liu S, Duan M. In-situ additive manufacturing deposition trajectory monitoring and compensation with thermal camera. Addit Manuf 2023; 78:103820. https://doi.org/10.1016/j.addma.2023.103820.